Direct observation of epitaxial alignment of Au on MoS₂ at atomic resolution

Yinghui Sun[1], Haofei Zhao[1], Dan Zhou[2], Yuchen Zhu[1], Huanyu Ye[1], Yan Aung Moe[1], and Rongming Wang[1] (✉)

[1] *Beijing Advanced Innovation Center for Materials Genome Engineering, Beijing Key Laboratory for Magneto-Photoelectrical Composite and Interface Science, School of Mathematics and Physics, University of Science and Technology Beijing, Beijing 100083, China*
[2] *Stuttgart Center for Electron Microscopy, Max Planck Institute for Solid State Research, Stuttgart 70569, Germany*

ABSTRACT

The morphology and structural stability of metal/2D semiconductor interfaces strongly affect the performance of 2D electronic devices and synergistic catalysis. However, the structural evolution at the interfaces has not been well explored particularly at atomic resolution. In this work, we study the structural evolution of Au nanoparticles (NPs) on few-layer MoS₂ by high resolution transmission electron microscopy (HRTEM) and quantitative high-angle annular dark field scanning TEM. It is found that in the transition of Au from nanoparticles to dendrites, a dynamically epitaxial alignment between Au and MoS₂ lattices is formed, and Moiré patterns can be directly observed in HRTEM images due to the mismatch between Au and MoS₂ lattices. This epitaxial alignment can occur in ambient conditions, and can also be accelerated by the irradiation of high-energy electron beam. *In situ* observation clearly reveals the rotation of Au NPs, the atom migration inside Au NPs, and the transfer of Au atoms between neighboring Au NPs, finally leading to the formation of epitaxially aligned Au dendrites on MoS₂. The structural evolution of metal/2D semiconductor interfaces at atomic scale can provide valuable information for the design and fabrication of the metal/2D semiconductor nano-devices with desired physical and chemical performances.

KEYWORDS

atom migration, MoS₂, *in situ* transmission electron microscopy (TEM), metal-semiconductor interface, Moiré patterns

1   Introduction

Two-dimensional (2D) semiconductors, such as semiconducting transition metal dichalcogenides (TMDs), have attracted growing interests owing to their promising physical and chemical properties [1–7], and shown great potentials in many charge-splitting applications [8–10]. In these applications, interfaces between metals and 2D semiconductors widely exist and play key roles in determining the efficiency of charge transport [11]. Extensive efforts have been devoted in the past years to study electrical [12–14], optoelectrical [15–18], and catalytic behaviors [19–23] of materials or devices with metal-2D semiconductor interfaces. It has been demonstrated that the morphology and structure of metals can dramatically modify the properties of 2D semiconductors, particularly when metals become nanostructured [24]. As the particle size decreases, the importance of morphology and structure stability increases, especially when the nanostructures are exposed to a complex environment [25, 26]. Therefore, it is essential to investigate the morphology and structural evolution of nanostructured metals on 2D semiconductors.

As a typical and stable material in the family of TMDs, MoS₂ has been employed to build versatile electronic devices [27–29]. Au is one of the most widely used electrode materials as contacts in the circuits of electronic devices. In addition, interfacing of MoS₂ with nanostructured Au has been used as active composites in electrochemical catalysis [19, 30]. The Au/MoS₂ interfaces strongly affect the performance of 2D electronic devices and synergistic catalysis. Direct observation of Au-MoS₂ interface is crucial to understand the nature of their interactions. Compared to the

studies of interface static morphology, dynamic evolution of the Au-MoS₂ interface is to some extent more important because Au is an easily mobile metal and thus the interface may change with time. Recently a few studies have reported the evolution of nanostructured Au on 2D materials [31–37], and some of them revealed the coalescence of chemically synthesized Au nanoparticles (NPs) on chemical-vapor-deposited graphene or mechanically exfoliated MoS₂ [31–33]. However, the principle of the interface evolution remains largely unknown, because either the relationship between Au and MoS₂ lattices or the transfer channel of Au atoms has yet to be observed in the evolution.

In this work, we *in situ* and quantitatively investigated the morphology and structural evolution of Au nanoparticles on MoS₂ by aberration-corrected transmission electron microscopy (TEM) and scanning TEM (STEM). We found that in the transition of Au from NPs to dendrites, an epitaxial alignment between Au and MoS₂ lattices is formed, and Moiré patterns with 2D honeycomb structures and 1D fringes can be directly observed in high-resolution TEM (HRTEM) images due to the mismatch between the Au and MoS₂ lattices. This epitaxial alignment can occur in ambient conditions, and can also be accelerated by the irradiation of high-energy electron beam. Further observation clearly reveals the rotation of Au NPs, the atom migration inside Au NPs, and the transfer of Au atoms between neighboring Au NPs, finally leading to the formation of epitaxially aligned Au dendrites on MoS₂. The temporal evolution in the spacing of Moiré fringes and the lattice parameter of Au on MoS₂ were also analyzed quantitatively. Our work provides comprehensive analyses on the structural and morphological evolution

---

Address correspondence to rmwang@ustb.edu.cn

of metal-2D semiconductor interfaces at atomic scale, which is essential to the design and fabrication of the metal-2D semiconductor nano-devices with desired performances.

2   Results and discussion

### 2.1   Structural evolution of Au NPs on MoS₂ under ambient conditions

Atomically thin MoS₂ flakes were mechanically exfoliated from bulk MoS₂ crystals onto Si substrates covered with a 300-nm-thick SiO₂ layer. Figure 1(a) shows an optical image of a local area with 3 layers (3L), 4 layers (4L), and bulk MoS₂. The number of layers was determined through both optical contrast and Raman spectrum. The interval between Raman in-plane mode E^1_{2g} and out-of-plane mode A_{1g} can be used as an indicator of the layer number of an ultrathin exfoliated MoS₂ flake [38, 39]. Figure 1(c) shows that the separations between E^1_{2g} and A_{1g} Raman modes are about 23.0 and 24.1 cm^{-1} (extracted by a Lorentzian peak fitting) for 3L and 4L MoS₂,

respectively, which are consistent with previous reports [38, 39]. Figure 1(b) shows an optical image of the MoS₂ flake transferred onto a gold TEM microgrid coated with a holey carbon film, where the 3L MoS₂ flake was tightly folded on top of the 4L one. Our TEM characterization was focused on the 4L part as indicated by the white dashed curves in Fig. 1(b). The MoS₂ flake with micrometer size is big enough for the TEM characterization. To compare the morphology and structural evolution of Au NPs on MoS₂, we characterized the same location with Au on 4L MoS₂, as indicated by the arrow at the bottom of Fig. 1(b) (unfolded part of MoS₂).

The few-layer MoS₂ on TEM grids were deposited with Au (2 nm in nominal thickness) by e-beam evaporation, and the schematic diagram of fabrication process was revealed in Fig. S1 in the Electronic Supplementary Material (ESM). The samples were immediately characterized in a vacuum chamber under TEM just after Au deposition, as shown in Fig. 2(b). The grids were then stored in dry N₂ box at room temperature after TEM characterization. The results of X-ray energy dispersive spectroscopy (EDS) of Au-MoS₂ in Fig. S2 in the ESM show that the elements in samples are Au, Mo and S.
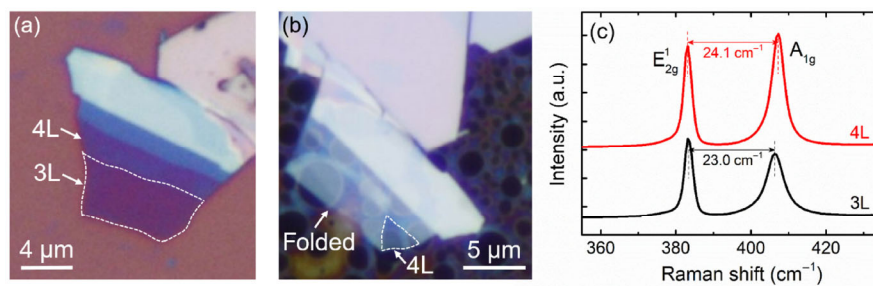
Figure 1 (a) Optical image of 3 and 4 layers (L), and thick MoS₂ flakes on SiO₂/Si wafer. (b) Optical image of the specific MoS₂ flake transferred on gold TEM grid with amorphous carbon film. Our TEM characterization was focused on the 4L part as indicated by the white dashed curves. (c) Representative Raman spectra excited by a 532-nm laser line of 3- and 4-layer MoS₂ flakes.
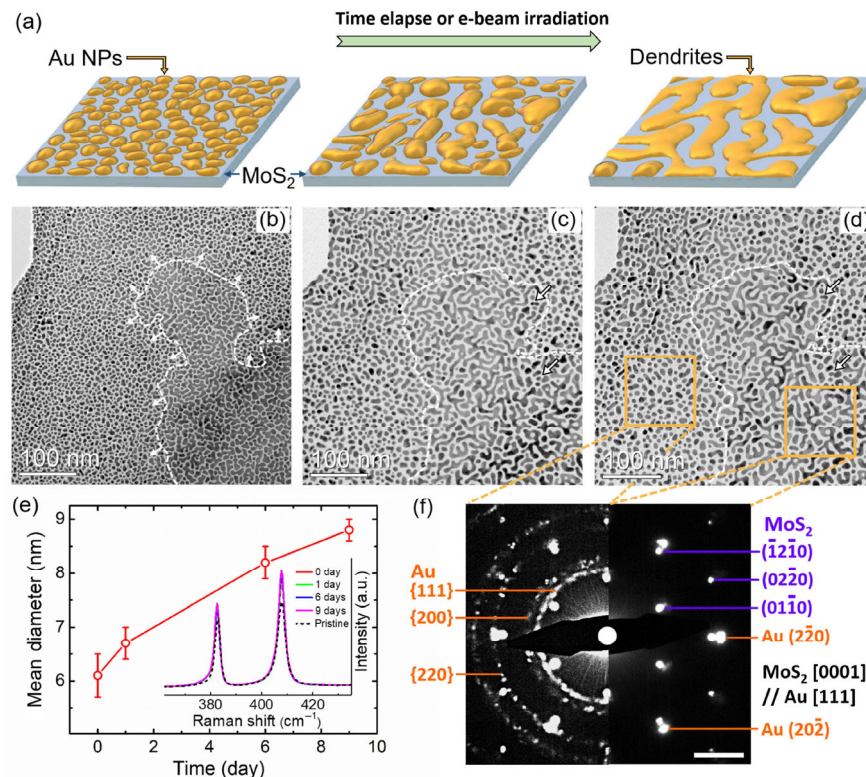
Figure 2 (a) The schematic diagrams of the transformation from Au NPs to dendrites with time elapse or electron beam irradiation. The blue substrate represents the MoS₂ flake. TEM images of Au on MoS₂ at the same location just after deposition (b), after 6 days (c), and after 9 days (d). The dashed white line marked the boundary between Au NPs and dendrites. (e) The time dependence of center diameters of Au NPs, changing from 6.1 to 8.8 nm. The statistic distributions of Au particle sizes were shown in Fig. S4 in the ESM. Inset: the time evolution of Raman spectra of 4-layer MoS₂ deposited with Au NPs on SiO₂/Si. No evident shift is observed in the Raman modes with time elapse. (f) SAED patterns for the NP and dendrite regions indicated by the orange frames in (d). The scale bar is 3 nm^{-1}.

The signal of copper may come from the TEM sample holder. The mapping image of Au (Fig. S2(c) in the ESM) is consistent with the STEM image of Au (marked by the yellow frame in Fig. S2(a) in the ESM), while the mapping images of S and Mo are homogenous in the mapping area, indicating the existence of MoS_2 substrate. Figures 2(c) and 2(d) show the bright field TEM images of the sample after 6 and 9 days. All the images exhibit two types of nanostructures: isolated NPs and short dendrites, while the fresh sample has more NPs and the stored one for 9 days has more dendrites. The boundaries of the NP and dendrite regions were marked by the white dashed lines. It is noted that the spacing between the NPs and the dendrites is well controlled, which is comparable with the characteristic length of the nanostructures. With the elapse of the storage time, the size of NPs and the width of the dendrites become larger, indicating the occurrence of a ripening process [40–42]. The schematic diagrams in Fig. 2(a) shows the transformation from Au NPs to dendrites with time elapse or the assistance of electron beam in TEM. For the fresh sample, the size of the NPs is measured to be about 6.1 nm, and the width of the dendrite is ~ 5.2 nm. The size of the NPs grows to ~ 8.2 and ~ 8.8 nm, and the width of the dendrite grows to ~ 6.8 and ~ 6.9 nm after 6 and 9 days' storage in N_2. The time dependence of the mean diameter of NPs is shown in Fig. 2(e). Particularly, some NPs transform into dendrites slowly, leading to the boundary of the two areas smoother as time elapse (Figs. 2(b) and 2(c)). The evolutions of both NPs and dendrites appear to slow down afterwards. After 9 days, the enlargement of the dendrite area is less noticeable, although the coalescence of NPs still occurs as indicated by white arrows in Figs. 2(c) and 2(d). The overview of sample morphologies at 0, 1, 6, and 9 days show a larger view of the evolution of morphology with time elapse (Fig. S3 in the ESM), further validating the coalescence of NPs and growth of dendrites.

Figure 2(f) shows selected-area electron diffraction (SAED) patterns obtained from Au NP region (left) and dendrite region (right). The complex SAED pattern from the Au NP region can be divided into three parts. The diffraction circles can be attributed to the Au NPs, indicating that most of them oriented randomly. The bright spots on the third circle can be attributed to {220} plane of Au, indicating the existence of Au NPs with preferential crystalline orientation along Au [111] zone axis. The bright spots within the first circle can be attributed to MoS_2 [0001]. However, the SAED pattern of Au NPs on amorphous carbon film (Fig. S5 in the ESM) only exhibits diffraction rings without any bright diffraction spots, indicating that the supporting MoS_2 flake is essential to the preferential orientated Au NPs. On the contrary, the complex SAED pattern

from the Au dendrite region in Fig. 2(f) (right) only consists of two parts, suggesting a well-epitaxial alignment between Au and MoS_2. Crystallographic analysis indicates that the orientation between Au and MoS_2 can be described by a typical crystallographic orientation relationship, $(11\bar{2}0)_{MoS_2}//(220)_{Au}$, $[0001]_{MoS_2}//[111]_{Au}$, which indicates that the closed directions of the two structures are parallel to each other. This result reveals that during the evolution of Au NPs into dendrites, the lattice direction of Au gradually evolves to match the [0001] direction of MoS_2. In this way, both the structures of Au and MoS_2 have three rotational symmetries, which is beneficial to lower the total energy of the heterostructure. We also measured Raman spectra of the sample for different storage time. No distinct difference can be observed in Raman spectra (inset of Fig. 2(e)), which indicates that Raman spectroscopy is not sensitive to the crystal orientation, despite of its sensitivity to local strain along the boundaries between metal NPs and MoS_2 [43]. Instead, TEM provides an efficient way for the evolution of metal-2D semiconductors interface.

2.2 Accelerated structural evolution of Au NPs under high energy electron beam irradiation

Dynamic high-resolution TEM investigations provide further insight into the evolution of the nanostructures. In our experiment, the images were taken at a dose rate of ~ 4.0×10^4 e$^-$/Å^2·s at 300 kV. We observed the evolutions of different Au NPs from tens to hundreds of seconds, respectively. The dynamic motions of Au NPs include the rotation of a single NP, the coalescence of two adjacent NPs, and the Ostwald ripening growth, etc. Figure 3 shows two typical dynamic motions of Au NPs on MoS_2: the rotation of an individual Au NP (Figs. 3(a)–3(d)) and the coalescing of two adjacent NPs (Figs. 3(e)–3(h)). As marked by white arrows in Figs. 3(a) and 3(b), the five interfaces of twin crystals depict a five-fold symmetry, which indicates that the pristine Au NP has an icosahedron structure randomly deposited on the surface of MoS_2. One (111) plane of one tetrahedron of the Au NP has a misorientation angle of ~ 17.2° with the $(11\bar{2}0)$ plane of MoS_2. After 44 s, the misorientation angle reduces to ~ 15.8°, revealing the rotation of the Au NP along MoS_2 [0001] direction (Fig. 3(b)). Meanwhile, the NP crystalline quality improves with the formation of facets of the tetrahedrons under the irradiation of the high-energy electron beam. Eventually, preferred crystalline orientations of Au NPs with MoS_2 forms after 455 s irradiation. As shown in Fig. 3(c), the Au (111) plane turns parallel to the $(11\bar{2}0)$ plane of MoS_2 without misorientation, which forms a semi-coherent interface with the closed planes of Au and MoS_2. The
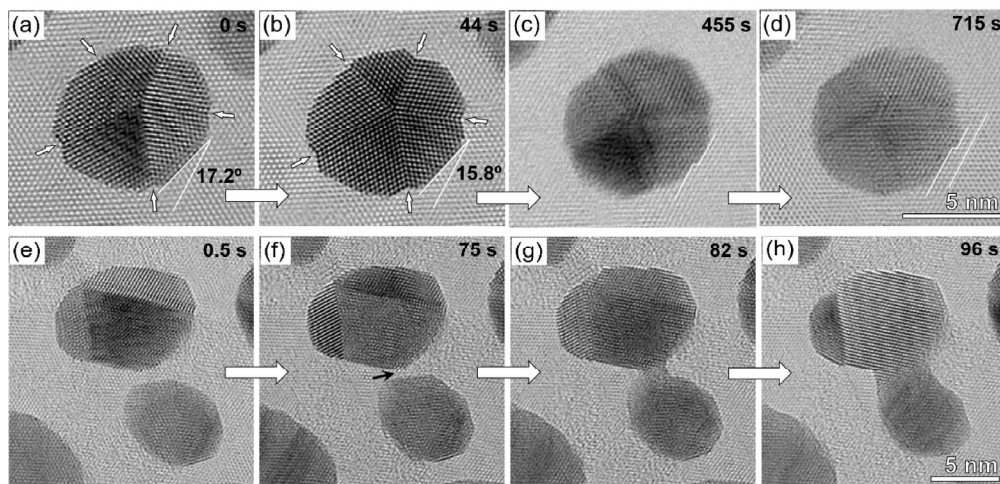
Figure 3 Two typical motions of the NPs on MoS_2: the rotation of an individual Au NP ((a)–(d)) and the coalescence of two adjacent NPs ((e)–(h)) with time record. White small arrows in (a) and (b) mark the five interfaces of twin crystals in the Au icosahedron. (a)–(d) have the same scale bar, as shown in (d); (e)–(h) have the same scale bar, as shown in (h).

atom diffusion on the surface of Au NPs also existed under the irradiation of high-energy electron beam. Under longer irradiation, the preferred crystalline orientation remains unchanged only with the migration of some outermost atoms (Fig. 3(d)), which indicates that the interface between Au and MoS$_2$ is stable with lowered energy. The migration of Au atoms could be captured by the shift of atom steps (Figs. 3(c) and 3(d)). Within 260 s, the outermost atom steps of the right-bottom tetrahedron in Fig. 3(c) was upshifted by 2–3 atom intervals, indicating the migration of Au atoms on the surface.

Figures 3(e)–3(h) reveal the coalescence of two adjacent NPs under the irradiation of electron beam. With the elapse of time, the position of the bigger NP remains almost fixed and the smaller NP moves into the bigger one. The gap distance between the two NPs gradually reduces from 0.86 to 0.26 nm after 75 s, and eventually disappeared after 82 s. As marked by a black arrow in Fig. 3(f), the darker contrast between the nearest points of the gap may come from the migration of Au atoms from the smaller NP (Fig. S6 in the ESM). Accompanying the atom migration of the smaller NP, the rotation of the bigger one also occurs, which can be illustrated from the change of diffraction contrasts in Figs. 3(e)–3(h). The migration channel may accelerate the coalescence process. At the first stage (Figs. 3(e) and 3(f)), the atom migration is relatively slow. However, once the atom channel forms, the two nearest NPs contact together within only several seconds (Figs. 3(f) and 3(g)). And then a part of dendrite structure was formed only after 14 s (Figs. 3(g) and 3(h)).

2.3 Direct observation of atom migration within and between Au NPs

The 3D atomic-scale change of the NP structures and their coalescence

under electron beam irradiation can be well resolved by quantitative high-angle annular dark field (HAADF) STEM imaging. The time-series HAADF images, shown in Figs. 4(a)–4(c), represent increased electron dose impinged to the sample area illuminated. The bridging of two initially separated NPs indicates the start of the coalescing process. In Fig. 4(a), the superimposed contrast in the gap (marked by a white arrow) may also be ascribed to the migration of Au atoms, similar to the HRTEM result in Fig. 3(f). Figure 4(b) shows a HAADF STEM image of the two NPs in the merging process. The missing of clear atomic features indicates a bit disordered state at the bridging interface. After 17 min, as shown in Fig. 4(c), a clear twin boundary between the two NPs are observed.

The counting of Au atom numbers in a NP at different electron irradiation dose through time-series quantitative HAADF STEM imaging gives the dynamic atom distribution and migration during the coalescence. From the selected serial STEM images of an Au NP in Figs. 4(e) and 4(f), the atom counting results can be obtained in Figs. 4(g) and 4(h). From the top view of Figs. 4(g) and 4(h), the apex atom of the icosahedron is absent, while a few atoms at the edges of icosahedron are deficient, which is similar to the surface structure of FePt NP [44, 45]. During the process of coalescence, the migration of outermost atoms to the boundary of the two NPs can be observed (Figs. 4(g) and 4(h)). It is noted that some of the surface atoms derive away from their equilibrium positions, forming bending planes as marked by white arrows in Fig. 4(h). Disordered structure with a thickness of about 2-atomic layers can be observed around the NP surface. Quantitative statistics reveals that the mean distances between the nearest atoms in Figs. 4(g) and 4(h) remain almost the same, which is ~ 2.94 Å with a full-width-at-half-maximum of ~ 0.23 Å. About 5% of the numbers of Au atoms have atomic
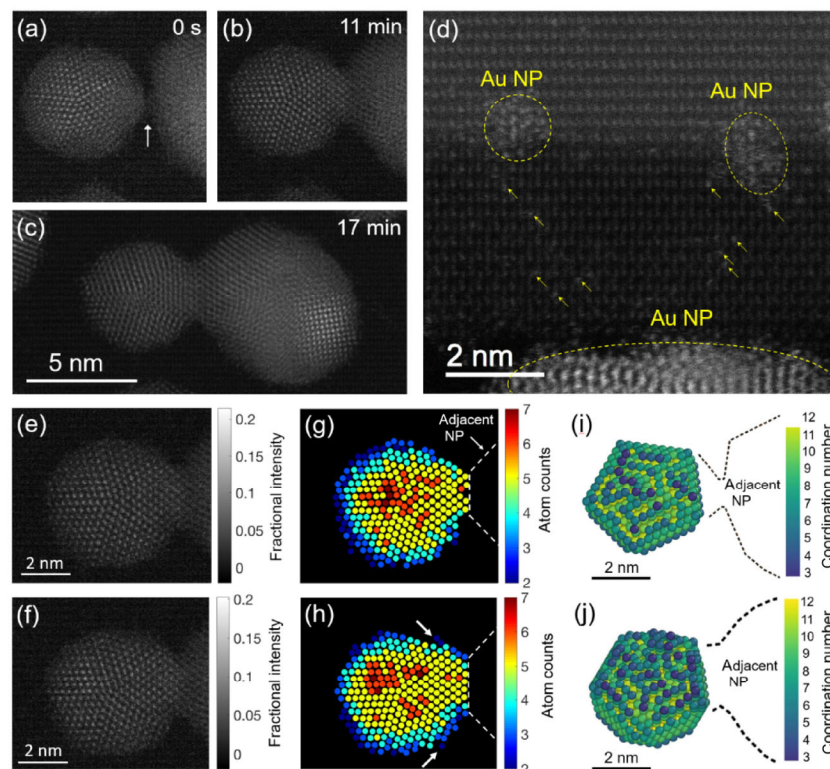
Figure 4 The coalescence process of Au NPs verified by atomic-resolution STEM (a)–(c). They have the same scale bar, as shown in (c). (d) The atomic-resolution HAADF STEM image showing matter transfer channels of Au atoms on MoS$_2$. Au NPs with different sizes are marked by the dashed circles. The isolated Au atoms are marked by yellow arrows. Two small Au NPs adhere to the edge of different layers of MoS$_2$, which can be identified by the *z*-contrast in STEM. (e) and (f) Selected serial STEM images for the atom counting. (g) and (h) The atom counting results of Au NP in (e) and (f), showing the atomic planes bending towards to migrating particle under electron beam illumination, as indicated by the white arrows in (h). The white dashed lines indicate the approximate profiles of the adjacent NP. The scale bars for (g) and (h) are the same as those in (e) and (f). (i) and (j) 3D atom models of the left particle at the stage of starting contact (a) and being merged together with the right particle (c) under e-beam irradiation, respectively. With the e-beam irradiation, the surface atoms with lower coordination number increase (indicated by darker colored atoms). The dashed lines marked the profiles of the adjacent NPs when they just contact with each other and merge together, respectively.

spacing over 3.15 Å due to the contribution from surface atoms. The bending of outermost atomic layer and the increased distances between the nearest surface atoms may be attributed to the electron beam irradiation and the attraction from the adjacent bigger NP. When the distance expansion increases to 10%, the atom is possible to detach from the NP [45], and become the material source for atomic channel. The matter transfer channels for Au atoms can be observed in STEM image, as shown in Fig. 4(d). The Au atoms are marked by yellow arrows, which may form atomic channel to realize matter transfer between the bigger Au NP at the bottom and the small Au NPs. The migration of Au atoms on MoS_2 is also observed in other STEM images (Fig. S7 in the ESM). The formation process of the matter transfer channels of Au atoms on MoS_2 is also revealed by the time series HAADF STEM images in Fig. S8 in the ESM.

From the quantitative analysis of the number of atoms in each column from HAADF STEM images, 3D reconstruction of atom models can be obtained [46, 47]. Figures 4(i) and 4(j) show the 3D atom models of the left particle at the stage of starting contact (Fig. 4(a)) and being merged together with the right particle (Fig. 4(c)) under e-beam irradiation, respectively. With the irradiation, the number of atoms with low coordination number increases (Fig. 4(j)), which confirms the migration of surface atoms. However, the overall coordination number increases due to the aggregation of the two NPs. The total number of atoms in the left particle increases, with the number of atoms in each column increasing, indicating the extra atoms mostly migrated from the right particle. This coalescence process actually exists and is competitive with the Ostwald ripening process, which is a thermodynamically-driven process with large particles to grow by the cost of the smaller particles shrinking [48, 49]. The migration of surface atoms, including the migration of Au atoms on MoS_2 (Fig. 4(d)) and from the nearby NPs (Figs. 4(a)–4(c)), may result in the formation of the dendrite structures.

The formation of Au NPs on MoS_2 by e-beam evaporation follows the Volmer-Weber island growth mode [50]. Atom clusters nucleate and grow on MoS_2 surface, forming isolated metal islands. As Au is a highly mobile material, its islands can change dynamically even near room temperature, where the large islands grow at the expense of the shrinking of small ones [50]. Pashley et al. demonstrated that Au deposited on crystalline MoS_2 flake have final grain sizes larger than the initial island spacing in *in situ* electron microscopy studies [35, 36], revealing a liquid-like behavior of the coalescence of the initial metal nuclei. Thermodynamically, the system of Au NPs should evolve towards the minimum of its total energy. Therefore, the system tends to coalesce to reduce the surface energy at Au-air or Au-vacuum interfaces, and reconstruct the crystalline orientations to minimize the elastic energy induced by the stress at the Au-MoS_2 interface due to their lattice mismatch. Kinetically, the atom diffusion of Au should overcome an energy barrier, and the driving force may originate from thermal fluctuation in ambient conditions (the case shown in Fig. 2) or inelastic scattering between the incident electron beam and the surface atoms under TEM (the case shown in Fig. 4). Coalescence of Au NPs has also been observed for both pristine and hydrogenated graphene as a result of long electron beam exposure [34]. For 2D materials, like graphene and MoS_2, there are few dangling bonds at the surface, and the interaction between Au and graphene or MoS_2 is weak. Thus the coalescence of Au NPs into larger particles or dendrites can be easily realized. The observed evolution of Au NPs at ambient conditions suggests that it is crucial to study the interface stability of metal and 2D materials under conventional working conditions. For the substrates of non-2D materials, if the interaction between Au and the substrate is strong, it is hard to observe the coalescence process. For example, on the amorphous carbon film in TEM grid, Au NPs were not coalescent into dendrites in our experiment (as shown in Fig. S9 in

the ESM). It was clear that the Au NPs on few-layer MoS_2 had evolved into dendrites, while those on amorphous carbon film still remained as isolated NPs (Fig. S9 in the ESM).

## 2.4 Formation of epitaxial alignment between Au and MoS_2 lattices

After sufficient coalescence and lattice relaxation, Au dendrites form and gradually grow bigger. In fact, the formation of dendrites could occur in the pristine sample just after ~ 1 h in ambient conditions, with relatively low proportion but without preferred crystalline orientation to MoS_2 (Fig. 2(b)). During the HRTEM observations, the proportion of Au dendrites on the MoS_2 was continuously increased with time proceeding. Finally, most of the Au NPs were found to transfer into dendrites. Figure 5 shows the typical TEM images of Au dendrites. Due to the mismatch between the Au and MoS_2 lattice, Moiré patterns can be observed directly in HRTEM images (Figs. 5(a) and 5(b)). As shown in Fig. 5(a), the Moiré fringes are mostly parallel to $(11\bar{2}0)_{MoS_2}$ planes with the maximum spacing D_{max} of ~ 16.63 Å and the mean spacing of ~ 15.86 Å. D is defined by the equation $D = d_1 d_2 \cos \alpha / |d_2 - d_1|$, where d_1 and d_2 are the lattice spacing of the two crystal planes that give rise to the Moiré pattern, α is the rotation angle of the Moiré pattern relative to the original crystal plane. Compared with the ductility of Au, the few-layer MoS_2 can be treated as a rigid suspended substrate with bulk lattice structure and the spacing of $(11\bar{2}0)$ planes 1.580 Å. Therefore, the spacing of $(2\bar{2}0)$ planes of Au is derived to be 1.443 Å. Then the lattice parameter of Au is calculated to be 4.081 Å, consistent with the unstrained lattice parameter of Au, 4.078 Å. The Moiré fringes are magnified by ~ 10.8 times relative to the spacing of $(11\bar{2}0)_{MoS_2}$ planes. Detailed analysis shows that rotation angles still exist between the Moiré fringes and the $(11\bar{2}0)_{MoS_2}$ planes. The angles distribute in a range of ±25.0°, which can be measured from the expansion of diffraction spots in the fast Fourier transform (FFT) images (inset of Fig. 5(a)). The corresponding rotation angle of $(11\bar{2}0)_{MoS_2}$ planes with respect to the $(2\bar{2}0)_{Au}$ planes is about 25.0°/
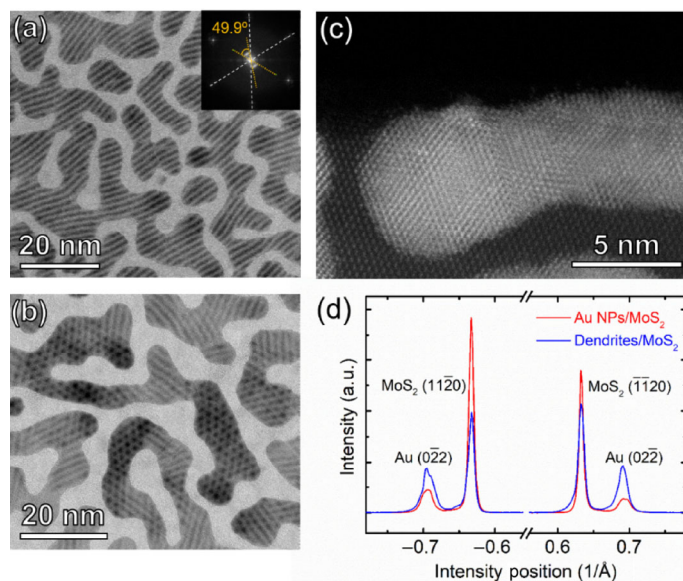
Figure 5 Two typical kinds of Moiré patterns in HRTEM images of Au dendrites on MoS_2 (a) and (b). Inset of (a): fast Fourier transform (FFT) of (a). The expansion of the diffraction spots near the center spot reflects the distribution of the rotation angles. The included angle between the two white dashed lines is measured to be 49.9°. Therefore, the rotation angles distribute in a range of ±25.0°. (c) The atomic-resolution STEM shows the lattice match of Au dendrite with MoS_2 lattice. (d) The extracted intensity profiles from SAED patterns of Au NPs/MoS_2 and dendrites/MoS_2 after calibrating the length by the lattice spacing of $(11\bar{2}0)$ planes of MoS_2. The lattice parameters of Au in NPs and dendrites can be derived respectively.

10.8 = 2.3°, showing that Au atoms have preferential crystalline orientations to the MoS_2 lattice. Under a specific condition, 2D Moiré patterns can also be observed, where the electron beam is strictly parallel to $[0001]_{MoS_2}//[111]_{Au}$. Figure 5(b) shows the typical hexagonal Moiré patterns. After several days' storage, the Au dendrites still maintain their morphologies. Dedicated measurement from the HRTEM image in Fig. 6(a) reveals that the mean spacing of Moiré fringes extended to ~ 16.80 Å. After 9 days' storage, the Au dendrites still maintain their morphologies, but the mean spacing of fringes increases compared with the mean spacing of Moiré fringes in pristine sample (~ 15.86 Å). The increase of fringe mean spacing indicated that the Au lattice parameter expands a little with the time elapse. Besides Moiré patterns in the pristine sample after e-beam irradiation for tens of minutes (shown in Figs. 5(a) and 5(b)), similar Moiré patterns were also observed in the samples stored in dry N_2 box at room temperature without the irradiation of electron beam (Fig. 6(b)). Au dendrites with preferential crystalline orientations to the MoS_2 lattice have lower energy and higher stability. The irradiation of electron beam can accelerate the formation of Au dendrites. Figure 5(c) shows the top-view atom arrangement of an Au dendrite and MoS_2 lattice, which is imaged by atomic-resolution STEM. It further validates that Au atoms indeed have preferential crystalline orientations to the MoS_2 lattice after relaxation. The Au dendrites with controllable formation under the e-beam irradiation may have potential applications as interconnects in nano- or molecular devices. The size-dependent grain-boundary structure in pure sub-10-nm gold nanorods has been studied recently [51].

From the SAED patterns of Au NPs/MoS_2 and dendrites/MoS_2, we can obtain the intensity profiles in the two cases, after calibrating the length by the lattice spacing of $(11\bar{2}0)$ planes of MoS_2 (Fig. 5(d)). The Au lattice parameters of NPs and dendrites are derived to be 4.075 and 4.087 Å, respectively, indicating that the metal lattice is expanded by ~ 0.3% with the interaction from the bottom MoS_2 lattice. This result indicates the strong impact from the rigid MoS_2 lattice on the lattice structure of the ductile Au nanostructures [52]. As Au is a highly mobile material, its NPs can merge dynamically into dendrites even near room temperature. The gap distance between Au NPs is a crucial parameter to affect the transformation from NPs to dendrites. In our experiment, the mean gap distance between NPs is about 5 nm, which is small enough to realize the dendrite formation at room temperature. This result further validates our analysis on the thermodynamic and kinetic mechanisms of the Au evolution on MoS_2. Previous study has shown that Au NPs have facet-dependent sintering behaviors on different surfaces of a crystal [53]. It is known that at edges of a MoS_2 flake, either Mo- or S-terminated surface exists and may have different adsorption energies with Au, which may drastically influence the evolution of Au NPs there. This leaves an interesting topic to study the evolution of Au NPs at the edges of a MoS_2 flake in our future work.
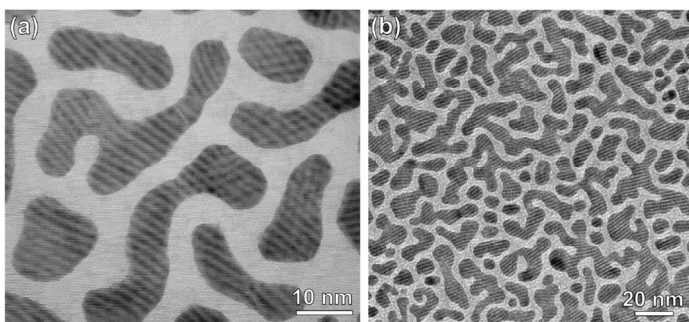
Figure 6 (a) HRTEM image of Au dendrites on MoS_2 after 9 days' storage. The mean spacing of the Moiré fringes is ~ 16.80 Å. (b) HRTEM image of Au dendrites on MoS_2 in the sample stored in dry N_2 at room temperature for several months without the irradiation of electron beam. Similar dendrite structure and Moiré patterns were also observed in this sample.

Ag is as mobile as Au, similar structural evolution may exist for Ag NPs on MoS_2, taken into account the same crystalline symmetry and similar lattice parameters of Au and Ag. But the Ag NPs are not as stable as Au NPs, and are easier to form Ag–S chemical bond between Ag and MoS_2. Therefore, the evolution of Ag NPs is more complicated. For other metals, it is also valuable to explore the possible interaction between metal and 2D materials. The migration and aggregation of Pd NPs on graphene has been reported [54]. Damaging of graphene has been observed in the presence of Al, Ti, Cr, and Ni, although their interaction with graphene varies [55]. The refacetting process of Pd NPs, induced by N_2 under atmospheric pressure at elevated temperatures, was observed by *in situ* TEM [56]. The etching of MoS_2 by Pt nanocrystals has also been reported at high temperature [52]. So the interaction of metal with 2D materials under different conditions has attracted much attention, and is a fundamental issue to gain a better understanding of the metal contacts and so on.

3 Conclusion

In summary, we have investigated the structural evolution of Au from NPs to dendrites on 2D MoS_2 thin layers. The Au NPs with polycrystalline structure can merge together with the assistance of electron beam, and rotate to match the lattice direction of MoS_2. Au dendrites with monocrystalline structure, can be formed on MoS_2 with distinctly periodic Moiré patterns, which indicates the strong epitaxial alignment between the crystal planes of $(11\bar{2}0)_{MoS_2}$ and $(220)_{Au}$. The atom-resolved morphology and structural evolution of Au NPs/MoS_2 in this alignment process was investigated by HRTEM and quantitative HAADF STEM. *In situ* TEM observation shows the migration of Au atoms on MoS_2 and the coalescence of adjacent NPs, which may lead to the formation of the dendritic structures. The paved channel of Au atom on MoS_2 can also be distinguished. The structural evolution of metal-2D semiconductor interfaces at atomic scale can provide valuable information for the design and fabrication of the metal-2D semiconductor nanodevices.

4 Experimental section

4.1 Sample preparation

Mechanically exfoliated MoS_2 flakes from bulk MoS_2 crystals were used for the merits of the surface cleanness and stability, i.e., few defects or dangling bonds, and variable thickness of MoS_2 flakes from single- to thick-layer. Atomically thin MoS_2 flakes were exfoliated onto Si substrates covered with a 300-nm-thick SiO_2 layer. The layer number of MoS_2 flakes was firstly identified by the optical contrasts, and further confirmed by Raman spectra where the interval between the in-plane mode E^1_{2g} and the out-of-plane mode A_{1g} was found to depend on the thickness of MoS_2. Gold microgrids coated with holey carbon films were used for TEM investigations. A nitrogen gun was used to blow and clean the surface of MoS_2 flakes before laying a TEM microgrid on top of them. After the blowing procedure, the 3L MoS_2 was folded. The microgrid was laid on the top of MoS_2 flake with carbon film side in contact, as shown in the schematic diagram of fabrication process in Fig. S1 in the ESM. A droplet of acetone was then applied to strengthen the adhesion between the microgrid and the flake. After that, a piece of polydimethylsiloxane (PDMS) was attached closely to the wafer with TEM grid. The sample was immersed in a 1 M KOH solution until the microgrid and the flake detached from the substrate. Finally, the microgrid with the flake was rinsed in DI water and then dried for Au deposition. Au was deposited using e-beam evaporation at a rate of 0.2 Å/s under 5×10^{-6} Torr base pressure. The nominal thickness of Au was monitored by a quartz crystal oscillator. To obtain the

proper sizes and gaps between Au NPs, a nominal thickness of about 2 nm was adopted in our current experiments. The samples were kept in a dry nitrogen box for storage.

4.2   Characterizations

Raman measurements were performed in air using a Raman spectrometer (Horiba Jobin Yvon HR800) with an excitation wavelength of 532 nm. Raman spectral resolution was ~ 1.5 cm^{-1}. A low laser power of ~ 200 μW was used to prevent overheating of MoS_2. The structure and morphology of the transferred samples were characterized by an image-aberration-corrected TEM (Titan ETEM G2) operated at 300 kV and a probe-aberration-corrected TEM (JEOL ARM-200F) operated at 200 kV.

4.3   Atom counting of Au nanoparticle

The experimental HAADF images were obtained using JEOL ARM-200F. The experimental convergence semi-angle was 21 mrad. The corresponding inner and outer collection semi-angles were set to 63–175 mrad. An individual frame of HAADF image were acquired with 2 μs/pixel, 1,024 × 1,024 pixels per frame (sampling of 0.18 Å/pixel), and a flyback time of 1,000 μs, which result in an acquisition time of 3.12 s/frame. The electron beam current was 14 pA, which gives a single frame dose of around 2.7×10^5 e$^-$/Å^2.

The as-acquired HAADF images were firstly normalized to a fractional intensity scale relative to the incident beam intensity, as required for a quantitative comparison with simulated HAADF images [57, 58]. The scattering from TEM grid carbon and supported MoS_2 was subtracted from the images before comparison to the simulations. A hybrid statistics-simulations based method for atom-counting from the HAADF images [59] was applied to determine each column's atom counts. The simulations presented in this paper were computed with the frozen phonon multi-slice method as implemented by Kirkland [60] with 15 phonon configurations. For comparison with experimental data, the detector sensitivity map was firstly normalized to the mean intensity of the detector map and multiplied with convergent-beam electron diffraction (CBED) pattern before integrating the CBED to HAADF intensity at that pixel.

Acknowledgements

Electronic Supplementary Material: Supplementary material (schematic diagram of the fabrication process, energy dispersive X-ray spectroscopy of Au deposited MoS_2, the overall morphologies of Au on MoS_2 at the same location with time elapse, Au particle size distributions, the TEM image and diffraction pattern of Au NPs on amorphous carbon, line profiles of the contrast between the nearest points of the gap in HRTEM images, the atomic-resolution HAADF STEM image showing matter transfer channels of Au atoms on MoS_2, the formation process of the matter transfer channels of Au atoms on MoS_2, HRTEM image showing the comparison of morphologies of Au on MoS_2 and amorphous carbon film) is available in the online version of this article at https://doi.org/10.1007/s12274-019-2329-4.

References

[1] Radisavljevic, B.; Radenovic, A.; Brivio, J.; Giacometti, V.; Kis, A. Single-layer MoS_2 transistors. *Nat. Nanotechnol.* **2011**, *6*, 147–150.

[2] Butler, S. Z.; Hollen, S. M.; Cao, L. Y.; Cui, Y.; Gupta, J. A.; Gutiérrez, H. R.; Heinz, T. F.; Hong, S. S.; Huang, J. X.; Ismach, A. F. et al. Progress,

[3] Fiori, G.; Bonaccorso, F.; Iannaccone, G.; Palacios, T.; Neumaier, D.; Seabaugh, A.; Banerjee, S. K.; Colombo, L. Electronics based on two-dimensional materials. *Nat. Nanotechnol.* **2014**, *9*, 768–779.

[4] Voiry, D.; Fullon, R.; Yang, J.; de Carvalho Castro e Silva, C.; Kappera, R.; Bozkurt, I.; Kaplan, D.; Lagos, M. J.; Batson, P. E.; Gupta, G. et al. The role of electronic coupling between substrate and 2D MoS_2 nanosheets in electrocatalytic production of hydrogen. *Nat. Mater.* **2016**, *15*, 1003–1009.

[5] Sun, Y. H.; Wang, R. M.; Liu, K. Substrate induced changes in atomically thin 2-dimensional semiconductors: Fundamentals, engineering, and applications. *Appl. Phys. Rev.* **2017**, *4*, 011301.

[6] Asres, G. A.; Baldovi, J. J.; Dombovari, A.; Järvinen, T.; Lorite, G. S.; Mohl, M.; Shchukarev, A.; Pérez Paz, A.; Xian, L. D.; Mikkola, J. P. et al. Ultrasensitive H_2S gas sensors based on p-type WS_2 hybrid materials. *Nano Res.* **2018**, *11*, 4215–4224.

[7] Wang, J. H.; Xu, X. Z.; Qiao, R. X.; Liang, J.; Liu, C.; Zheng, B. H.; Liu, L.; Gao, P.; Jiao, Q. Z.; Yu, D. P. et al. Visualizing grain boundaries in monolayer $MoSe_2$ using mild H_2O vapor etching. *Nano Res.* **2018**, *11*, 4082–4089.

[8] Wang, Q. H.; Kalantar-Zadeh, K.; Kis, A.; Coleman, J. N.; Strano, M. S. Electronics and optoelectronics of two-dimensional transition metal dichalcogenides. *Nat. Nanotechnol.* **2012**, *7*, 699–712.

[9] Koppens, F. H. L.; Mueller, T.; Avouris, P.; Ferrari, A. C.; Vitiello, M. S.; Polini, M. Photodetectors based on graphene, other two-dimensional materials and hybrid systems. *Nat. Nanotechnol.* **2014**, *9*, 780–793.

[10] Jariwala, D.; Sangwan, V. K.; Lauhon, L. J.; Marks, T. J.; Hersam, M. C. Emerging device applications for semiconducting two-dimensional transition metal dichalcogenides. *ACS Nano* **2014**, *8*, 1102–1120.

[11] Xu, Y.; Cheng, C.; Du, S. C.; Yang, J. Y.; Yu, B.; Luo, J.; Yin, W. Y.; Li, E. P.; Dong, S. R.; Ye, P. D. et al. Contacts between two- and three-dimensional materials: Ohmic, Schottky, and p-n heterojunctions. *ACS Nano* **2016**, *10*, 4895–4919.

[12] He, Q. Y.; Zeng, Z. Y.; Yin, Z. Y.; Li, H.; Wu, S. X.; Huang, X.; Zhang, H. Fabrication of flexible MoS_2 thin-film transistor arrays for practical gas-sensing applications. *Small* **2012**, *8*, 2994–2999.

[13] Shi, Y. M.; Huang, J. K.; Jin, L. M.; Hsu, Y. T.; Yu, S. F.; Li, L. J.; Yang, H. Y. Selective decoration of Au nanoparticles on monolayer MoS_2 single crystals. *Sci. Rep.* **2013**, *3*, 1839.

[14] Sreeprasad, T. S.; Nguyen, P.; Kim, N.; Berry, V. Controlled, defect-guided, metal-nanoparticle incorporation onto MoS_2 via chemical and microwave routes: Electrical, thermal, and structural properties. *Nano Lett.* **2013**, *13*, 4434–4441.

[15] Kang, Y. M.; Najmaei, S.; Liu, Z.; Bao, Y. J.; Wang, Y. M.; Zhu, X.; Halas, N. J.; Nordlander, P.; Ajayan, P. M.; Lou, J. et al. Plasmonic hot electron induced structural phase transition in a MoS_2 monolayer. *Adv. Mater.* **2014**, *26*, 6467–6471.

[16] Li, Z.; Xiao, Y.; Gong, Y.; Wang, Z.; Kang, Y.; Zu, S.; Ajayan, P. M.; Nordlander, P.; Fang, Z. Active light control of the MoS_2 monolayer exciton binding energy. *ACS Nano* **2015**, *9*, 10158–10164.

[17] Miao, J. S.; Hu, W. D.; Jing, Y. L.; Luo, W. J.; Liao, L.; Pan, A. L.; Wu, S. W.; Cheng, J. X.; Chen, X. S.; Lu, W. Surface plasmon-enhanced photodetection in few layer MoS_2 phototransistors with Au nanostructure arrays. *Small* **2015**, *11*, 2392–2398.

[18] Gong, L. L.; Zhang, Q.; Wang, L. J.; Wu, J. F.; Han, C.; Lei, B.; Chen, W.; Eda, G.; Goh, K. E. J.; Sow, C. H. Emergence of photoluminescence on bulk MoS_2 by laser thinning and gold particle decoration. *Nano Res.* **2018**, *11*, 4574–4586.

[19] Kim, J.; Byun, S.; Smith, A. J.; Yu, J.; Huang, J. X. Enhanced electrocatalytic properties of transition-metal dichalcogenides sheets by spontaneous gold nanoparticle decoration. *J. Phys. Chem. Lett.* **2013**, *4*, 1227–1232.

[20] Wang, J. H.; Yan, M. Y.; Zhao, K. N.; Liao, X. B.; Wang, P. Y.; Pan, X. L.; Yang, W.; Mai, L. Q. Field effect enhanced hydrogen evolution reaction of MoS_2 nanosheets. *Adv. Mater.* **2017**, *29*, 1604464.

[21] Huang, X.; Zeng, Z. Y.; Bao, S. Y.; Wang, M. F.; Qi, X. Y.; Fan, Z. X.; Zhang, H. Solution-phase epitaxial growth of noble metal nanostructures on dispersible single-layer molybdenum disulfide nanosheets. *Nat. Commun.* **2013**, *4*, 1444.

[22] Yan, M. Y.; Zhou, X. B.; Pan, X. L.; Wang, J. H.; Xia, L. X.; Yu, K. S.; Liao, X. B.; Xu, X.; He, L.; Mai, L. Q. Electric field and photoelectrical effect bi-enhanced hydrogen evolution reaction. *Nano Res.* **2018**, *11*, 3205–3212.

[23] Zhang, J.; Wu, J. J.; Guo, H.; Chen, W. B.; Yuan, J. T.; Martinez, U.; Gupta, G.; Mohite, A.; Ajayan, P. M.; Lou, J. Unveiling active sites for the hydrogen evolution reaction on monolayer MoS₂. *Adv. Mater.* **2017**, *29*, 1701955.

[24] Moe, Y. A.; Sun, Y. H.; Ye, H. Y.; Liu, K.; Wang, R. M. Probing evolution of local strain at MoS₂-metal boundaries by surface-enhanced Raman scattering. *ACS Appl. Mater. Interfaces* **2018**, *10*, 40246–40254.

[25] Jiang, Y.; Wang, Y.; Zhang, Y. Y.; Zhang, Z. F.; Yuan, W. T.; Sun, C. H.; Wei, X.; Brodsky, C. N.; Tsung, C. K.; Li, J. X. et al. Direct observation of Pt nanocrystal coalescence induced by electron-excitation-enhanced van der Waals interactions. *Nano Res.* **2014**, *7*, 308–314.

[26] Jiang, Y.; Zhang, Z. F.; Yuan, W. T.; Zhang, X.; Wang, Y.; Zhang, Z. Recent advances in gas-involved *in situ* studies via transmission electron microscopy. *Nano Res.* **2018**, *11*, 42–67.

[27] Perera, M. M.; Lin, M. W.; Chuang, H. J.; Chamlagain, B. P.; Wang, C. Y.; Tan, X. B.; Cheng, M. M. C.; Tománek, D.; Zhou, Z. X. Improved carrier mobility in few-layer MoS₂ field-effect transistors with ionic-liquid gating. *ACS Nano* **2013**, *7*, 4449–4458.

[28] Perkins, F. K.; Friedman, A. L.; Cobas, E.; Campbell, P. M.; Jernigan, G. G.; Jonker, B. T. Chemical vapor sensing with monolayer MoS₂. *Nano Lett.* **2013**, *13*, 668–673.

[29] Lopez-Sanchez, O.; Lembke, D.; Kayci, M.; Radenovic, A.; Kis, A. Ultrasensitive photodetectors based on monolayer MoS₂. *Nat. Nanotechnol.* **2013**, *8*, 497–501.

[30] Hussain, M. A.; Yang, M.; Lee, T. J.; Kim, J. W.; Choi, B. G. High density decoration of noble metal nanoparticles on polydopamine-functionalized molybdenum disulphide. *J. Colloid Interface Sci.* **2015**, *451*, 216–220.

[31] Yuk, J. M.; Jeong, M.; Kim, S. Y.; Seo, H. K.; Kim, J.; Lee, J. Y. *In situ* atomic imaging of coalescence of au nanoparticles on graphene: Rotation and grain boundary migration. *Chem. Commun.* **2013**, *49*, 11479–11481.

[32] Zhou, H. Q.; Yu, F.; Guo, C. F.; Wang, Z. P.; Lan, Y. C.; Wang, G.; Fang, Z. Y.; Liu, Y.; Chen, S.; Sun, L. F. et al. Well-oriented epitaxial gold nanotriangles and bowties on MoS₂ for surface-enhanced Raman scattering. *Nanoscale* **2015**, *7*, 9153–9157.

[33] Kiriya, D.; Zhou, Y. Z.; Nelson, C.; Hettick, M.; Madhvapathy, S. R.; Chen, K.; Zhao, P. D.; Tosun, M.; Minor, A. M.; Chrzan, D. C. et al. Oriented growth of gold nanowires on MoS₂. *Adv. Funct. Mater.* **2015**, *25*, 6257–6264.

[34] Zan, R.; Bangert, U.; Ramasse, Q.; Novoselov, K. S. Evolution of gold nanostructures on graphene. *Small* **2011**, *7*, 2868–2872.

[35] Pashley, D. W.; Stowell, M. J.; Jacobs, M. H.; Law, T. J. The growth and structure of gold and silver deposits formed by evaporation inside an electron microscope. *Philos. Mag.* **1964**, *10*, 127–158.

[36] Pashley, D. W.; Stowell, M. J. Nucleation and growth of thin films as observed in the electron microscope. *J. Vac. Sci. Technol.* **1966**, *3*, 156–166.

[37] Takayanagi, K.; Tanishiro, Y.; Yagi, K.; Kobayashi, K.; Honjo, G. UHV-TEM study on the reconstructed surface of Au(111): Metastable p" × p" and stable p × 1 surface structure. *Surf. Sci.* **1988**, *205*, 637–651.

[38] Lee, C.; Yan, H. G.; Brus, L. E.; Heinz, T. F.; Hone, J.; Ryu, S. Anomalous lattice vibrations of single- and few-layer MoS₂. *ACS Nano* **2010**, *4*, 2695–2700.

[39] Li, H.; Zhang, Q.; Yap, C. C. R.; Tay, B. K.; Edwin, T. H. T.; Olivier, A.; Baillargeat, D. From bulk to monolayer MoS₂: Evolution of Raman scattering. *Adv. Funct. Mater.* **2012**, *22*, 1385–1390.

[40] Wen, J. M.; Evans, J. W.; Bartelt, M. C.; Burnett, J. W.; Thiel, P. A. Coarsening mechanisms in a metal film: From cluster diffusion to vacancy ripening. *Phys. Rev. Lett.* **1996**, *76*, 652–655.

[41] Pai, W. W.; Swan, A. K.; Zhang, Z. Y.; Wendelken, J. F. Island diffusion and coarsening on metal (100) surfaces. *Phys. Rev. Lett.* **1997**, *79*, 3210–3213.

[42] Stoldt, C. R.; Jenks, C. J.; Thiel, P. A.; Cadilhe, A. M.; Evans, J. W. Smoluchowski ripening of Ag islands on Ag(100). *J. Chem. Phys.* **1999**, *111*, 5157–5166.

[43] Sun, Y. H.; Liu, K.; Hong, X. P.; Chen, M.; Kim, J.; Shi, S. F.; Wu, J. Q.; Zettl, A.; Wang, F. Probing local strain at MX₂-metal boundaries with surface plasmon-enhanced Raman scattering. *Nano Lett.* **2014**, *14*, 5329–5334.

[44] Wang, R. M.; Dmitrieva, O.; Farle, M.; Dumpich, G.; Ye, H. Q.; Poppa, H.; Kilaas, R.; Kisielowski, C. Layer resolved structural relaxation at the surface of magnetic FePt icosahedral nanoparticles. *Phys. Rev. Lett.* **2008**, *100*, 017205.

[45] Wang, R. M.; Dmitrieva, O.; Farle, M.; Dumpich, G.; Acet, M.; Mejia-Rosales, S.; Perez-Tijerina, E.; Yacaman, M. J.; Kisielowski, C. FePt icosahedra with magnetic cores and catalytic shells. *J. Phys. Chem. C* **2009**, *113*, 4395–4400.

[46] Liu, W.; Wang, N.; Wang, R. M.; Kumar, S.; Duesberg, G. S.; Zhang, H. Z.; Sun, K. Atom-resolved evidence of anisotropic growth in ZnS nanotetrapods. *Nano Lett.* **2011**, *11*, 2983–2988.

[47] Liu, J. L.; Liu, W.; Sun, Q.; Wang, S. G.; Sun, K.; Schwank, J.; Wang, R. M. *In situ* tracing of atom migration in Pt/NiPt hollow spheres during catalysis of Co oxidation. *Chem. Commun.* **2014**, *50*, 1804–1807.

[48] Alloyeau, D.; Prévot, G.; Le Bouar, Y.; Oikawa, T.; Langlois, C.; Loiseau, A.; Ricolleau, C. Ostwald ripening in nanoalloys: When thermodynamics drives a size-dependent particle composition. *Phys. Rev. Lett.* **2010**, *105*, 255901.

[49] Prévot, G.; Nguyen, N. T.; Alloyeau, D.; Ricolleau, C.; Nelayah, J. Ostwald-driven phase separation in bimetallic nanoparticle assemblies. *ACS Nano* **2016**, *10*, 4127–4133.

[50] Seel, S. C. Stress and structure evolution during Volmer-Weber growth of thin films. Ph.D. Dissertation, MIT, Cambridge, 2002.

[51] Wang, C. Y.; Du, K.; Song, K. P.; Ye, X. L.; Qi, L.; He, S. Y.; Tang, D. M.; Lu, N.; Jin, H. J.; Li, F. et al. Size-dependent grain-boundary structure with improved conductive and mechanical stabilities in sub-10-nm gold crystals. *Phys. Rev. Lett.* **2018**, *120*, 186102.

[52] Wang, S. S.; Sawada, H.; Chen, Q.; Han, G. G. D.; Allen, C.; Kirkland, A. I.; Warner, J. H. *In situ* atomic-scale studies of the formation of epitaxial Pt nanocrystals on monolayer molybdenum disulfide. *ACS Nano* **2017**, *11*, 9057–9067.

[53] Yuan, W. T.; Zhang, D. W.; Ou, Y.; Fang, K.; Zhu, B. E.; Yang, H. S.; Hansen, T. W.; Wagner, J. B.; Zhang, Z.; Gao, Y. et al. Direct *in situ* TEM visualization and insight into the facet-dependent sintering behaviors of gold on TiO₂. *Angew. Chem., Int. Ed.* **2018**, *57*, 16827–16831.

[54] Jin, Z.; Nackashi, D.; Lu, W.; Kittrell, C.; Tour, J. M. Decoration, migration, and aggregation of palladium nanoparticles on graphene sheets. *Chem. Mater.* **2010**, *22*, 5695–5699.

[55] Zan, R.; Bangert, U.; Ramasse, Q.; Novoselov, K. S. Interaction of metals with suspended graphene observed by transmission electron microscopy. *J. Phys. Chem. Lett.* **2012**, *3*, 953–958.

[56] Zhang, X.; Meng, J.; Zhu, B. E.; Yuan, W. T.; Yang, H. S.; Zhang, Z.; Gao, Y.; Wang, Y. Unexpected refacetting of palladium nanoparticles under atmospheric N₂ conditions. *Chem. Commun.* **2018**, *54*, 8587–8590.

[57] LeBeau, J. M.; Findlay, S. D.; Allen, L. J.; Stemmer, S. Quantitative atomic resolution scanning transmission electron microscopy. *Phys. Rev. Lett.* **2008**, *100*, 206101.

[58] LeBeau, J. M.; Stemmer, S. Experimental quantification of annular dark-field images in scanning transmission electron microscopy. *Ultramicroscopy* **2008**, *108*, 1653–1658.

[59] De Wael, A.; De Backer, A.; Jones, L.; Nellist, P. D.; van Aert, S. Hybrid statistics-simulations based method for atom-counting from ADF STEM images. *Ultramicroscopy* **2017**, *177*, 69–77.

[60] Kirkland, E. J. *Advanced computing in electron microscopy*; Boston, MA: Springer, 2010.